Journal of Materials Chemistry C

ARTICLE

An Efficient synthetic Strategy for Uniform Perovskite Core-Shell Nanocubes $NaMgF_3:Mn^{2+}$, Yb^{3+}@$NaMgF_3:Yb^{3+}$ with Enhanced Near Infrared Upconversion Luminescence

Received 00th January 20xx,
Accepted 00th January 20xx

DOI: 10.1039/x0xx00000x

www.rsc.org/

S. Ding,[a#] X. F. Yang,[b#] E. H. Song,[a] C. L. Liang,[c] B. Zhou,[a] M. M. Wu,[c] W. Z. Zhou,[d] and Q. Y. Zhang*[a]

Uniform perovskite core-shell nanocubes $NaMn_{1-x}Mg_xF_3$@$NaMgF_3$ and $NaMn_{1-x}Mg_xF_3:Yb^{3+}$@$NaMgF_3:Yb^{3+}$ have been successfully synthesized via a facile one-pot co-precipitation method at room temperature. The core-shell structures were carefully characterized by powder X-ray diffraction, transmission electron microscopy, scanning transmission electron microscopy and energy-dispersive X-ray elemental mapping. It was found that the formation mechanisms of the novel core-shell structures consisting of aggregation of precursor molecules/ions, multiple nucleation, surface re-crystallization and further phase transformation. In addition, the DFT calculations further showed that Mn^{2+} ions tend to aggregate in $NaMgF_3:Mn^{2+}$, and which may be one of important intrinsic factors for formation the unique $NaMn_{1-x}Mg_xF_3$@$NaMgF_3$ structure in this case. Besides, the unique core-shell structures $NaMn_{1-x}Mg_xF_3:Yb^{3+}$@$NaMgF_3:Yb^{3+}$ can obviously enhance near-infrared upconversion luminescence of Mn^{2+}, that may find high potential in multiple high-resolution imaging applications.

1. Introduction

Hierarchical design of core-shell nanoparticles provides a range of unique physicochemical properties through incorporating all the merits of different core-shell materials and thereby contributes to new applications.[1-4] Particularly, most of the recent exciting discoveries in this field show a tremendous scope for biomedical applications such as bioimaging, targeted drug delivery, biosensors, and diagnostics.[5-8] Besides, the core-shell strategy of the photon up-converting nanostructures can effectively suppress the luminescence quenching effect and greatly enhance the photon emission, making the materials much beneficial for bioimaging and biophotonic applications, which have received increasing attention.[9-13] One of the most common methods for fabricating these luminescent core-shell nanoparticles is the seed-mediated shell growth, namely, the core-only nanoparticles are firstly prepared as seeds for epitaxial growing of a homogeneous or heterogeneous shell on the surface of the seeds.[14-17] Despite monodispersed core-shell nanoparticles with diverse compositions can be easily obtained by using the seed- mediated shell growth approach, the method usually suffers from some limitations, including independent nucleation, anisotropic shell growth, and complicated separation and washing steps associated with multiple reactions. Therefore, it is highly desirable to develop a facile and environmentally friendly strategy for the preparation of well-defined and uniform core-shell crystals.

The Mn^{2+} activated phosphors are crucial for lighting and displays systems, due to their unique and tunable single band visible (VIS) emission characteristics.[18-22] According to the energy level diagrams for Mn^{2+}, its emission wavelength can be easily tuned from green to deep red region depending strongly on the crystal field environment.[23-25] For instance, the tetrahedrally coordinated Mn^{2+} with weaker crystal field strength usually gives green emission, whereas the octahedrally coordinated Mn^{2+} with stronger crystal field strength generally exhibits red emission. Most recently, it was found that the Mn^{2+} ions can not only give visible emission but also near infrared (NIR) emission, due to the Mn^{2+} aggregation induced formation of new emission center, super-exchange coupled Mn^{2+}-Mn^{2+} dimer, at a relative heavy Mn^{2+}-concentration.[23, 24] By codoping with Yb^{3+} in a suitable host lattice, $K(Zn, Mg)F_3:Mn^{2+}$, we can further achieve NIR UC emission, which may find potential applications in high-resolution bioimaging.[23] Moreover, as Mn^{2+} ions own five unpaired d electrons, the Mn^{2+} related nanocrystal can also be applied as an efficient T_1 magnetic resonance imaging (MRI) contrast agent, especially for Mn^{2+} concentrated compound.[26]

[a] State Key Laboratory of Luminescent Materials and Devices, and Institute of Optical Communication Materials, South China University of Technology, Guangzhou 510640, P. R. China
[b] Analytical and Testing Center, South China University of Technology, Guangzhou 510640, P. R. China
[c] School of Chemistry and Chemical Engineering, and Instrumental Analysis and Research Centre, Sun Yat-Sen (Zhongshan) University, Guangzhou 510275, P. R. China
[d] EaStCHEM, School of Chemistry, University of St Andrews, St Andrews, Fife KY16 9ST, United Kingdom
*Corresponding author: qyzhang@scut.edu.cn
# The two authors contributed equally to this work

Thus, the development of new core-shell nanostructures with Mn^{2+}-related NIR UC emission is not only important for fundamental research, but also be beneficial for multiple high-resolution imaging applications.

Herein, a new one-pot co-precipitation method is present for synthesizing perovskite $NaMn_{1-x}Mg_xF_3$@$NaMgF_3$ and core-shell $NaMn_{1-x}Mg_xF_3$:Yb^{3+}@$NaMgF_3$:Yb^{3+} nanocubes at room temperature without using any pre-synthesized templates or structure-directing surfactants. The formation mechanism or luminescent properties of the novel core-shell nano structures have been carefully investigated. The novel core-shell structure can obviously enhance the NIR UC emission of Mn^{2+}. Based on the systematic investigations of the formation dynamics and DFT calculations, a new mechanism for the growth of these nano core-shell structures has been proposed. The present work not only presents a new and environmentally friendly strategy to construct core-shell structure, but also provides efficient approach to enhance the NIR UC emission of Mn^{2+}.

2. Experimental

2.1. Raw materials

Manganese acetate tetrahydrate (99.9%), magnesium acetate tetrahydrate (99.9%), sodium fluoride (99.9%) and ytterbium oxide (99.99%) were purchased from Aladdin Industrial Corporation and used without further purification. 0.05 mol/L $Yb(NO_3)_3$ were prepared by dissolving a calculated amount of the corresponding ytterbium oxide into concentrated HNO_3 with gradual heating. De-ionized water was used in all the experiments.

2.2. Synthesis of core-shell nanocubes

In a typical synthesis of $NaMn_{1-x}Mg_xF_3$@$NaMgF_3$ core-shell nanocubes, a mixture of metal acetate tetrahydrate (4 mmol in total) with a molar ratio (Mn^{2+}: Mg^{2+} = 1 : 4) was dissolved into 5 mL of water and mixed with absolute ethanol (5 mL) to form a clear solution. 20 mL aqueous solution of sodium fluoride (0.7 mol/L) were then added dropwise to the solution with continuous stirring to maintain a slight excess of fluoride ions with respect to the metal acetate (M^{2+}: F^- = 1 : 3.5). The mixture was agitated for 15 min and then maintained at room temperature for 24 h. The product was isolated by centrifugation and washed several times with water and absolute ethanol to remove impurities, and finally dried at 60 °C for 12 h. To examine the detailed formation mechanism, aliquots were collected immediately at several reaction stage intervals after adding a definite amount of NaF solution, e.g., 10, 12.5, 15, and 17.5 mL.

2.3. Synthesis of Yb^{3+} doped core-shell nanocubes

To obtain the upconversion (UC) luminescence, we introduced the Yb^{3+} ions to the core-shell nanocubes as sensitizers with a sufficient absorption cross-section in the near-infrared region (976 nm). The synthesis process was similar to the above-mentioned process for the core-shell nanocubes, except that another 0.4 mL of 0.05 mol/L $Yb(NO_3)_3$ solution was added to the solutions at the initial stage. The as-grown white powder used as precursor was annealed under a N_2 atmosphere at 350 °C for 2 h to further improve their crystallinity and upconversion luminescence.

2.4. Synthesis of homogeneous solid-solution and physically mixed biphasic sample

To compare the upconversion luminescence properties of the core-shell nanocubes with that of conventional samples, a homogenous solid-solution and physically mixed biphasic sample were also prepared. The synthesis procedure of the former was similar to the procedure for the core-shell nanocubes with the nominal ratio of Mn^{2+}: Mg^{2+} = 1 : 4, except that the NaF solution was added rapidly to the acetate solution rather than dropwise addition as described above. The procedure of the preparation of the physically mixed samples was modified to yield the selected stoichiometric ratios of separately synthesized $NaMgF_3$: 0.5 mol% Yb^{3+} and $NaMnF_3$: 0.5 mol% Yb^{3+} powder samples, which were directly mixed and ground for 10 min using a pestle and mortar. The resulting samples were annealed under the same conditions as the process for the Yb^{3+} doped core-shell nanoparticles to improve the upconversion for comparison.

2.5. Theoretical calculations

Theoretical calculations were made based on the density functional theory (DFT) implemented in the Vienna ab initio simulation package (vasp).[27-29] The exchange correlation potential was approximated by generalized gradient approximation (GGA) with the PBE functional.[30] To evaluate the Mn^{2+} distribution in fluoride $NaMgF_3$:Mn^{2+}, a 2×2×2 $NaMgF_3$ supercell was constructed according to the ICSD card of No.90283, and the optimized parameters were given in Table S1. As two Mg^{2+} ions were replaced by two Mn^{2+} ions in the optimized 2×2×2 $NaMgF_3$ supercell, there were 15 different configurations (Figures S1 and S2). The cutoff energy Ecut and K-point mesh were set as 500 eV with a 1×1×1 Monkhorst-Pack grid, which are enough for energy convergence. The convergence criterion for the electronic energy was 10^{-4} eV and the structures were relaxed until the Hellmann–Feynman forces were less than 0.02 eV $Å^{-1}$.[31]

2.6. Specimen characterization

The crystal structures were initially determined using a Philips Model PW1830 X-ray powder diffractometer with Cu-Kα radiation (λ = 1.5406 Å) at 40 kV tube voltage and 40 mA tube current. The XRD profiles were refined using the Rietveld method with Topas Academic software (A. A. Coelho, TOPAS Academic V4, Coelho Software, Brisbane, Australia, 2005). The morphology of the samples was observed by scanning electron microscopy (SEM) on a Nova Nano 430 scanning electron microscope. Particle size distributions were obtained from the micrographs by counting several hundred particles. Transmission electron microscopy (TEM) images were obtained with a JEOL JEM-2100F microscope operating at 200 kV. High resolution TEM (HRTEM) images, scanning transmission electron microscopy (STEM) images and elemental mapping were obtained using an FEI Tecnai G2 F30 microscope operating at 300 kV equipped with a high angle annual dark field (HAADF) detector and an energy-dispersive X-

ray (EDX) spectrometer. The upconversion emission spectra were recorded on a TRIAX320 fluorescence spectrofluorometer (Jobin-Yvon Co., France) equipped with a R928 photomultiplier tube as the detector and a 976 nm laser diode (Coherent Corp.) as the excitation source. Fourier-transform IR spectra (FT-IR) were recorded on a VERTEX 70 IR spectrophotometer using the KBr pellet method. The accurate Mn^{2+}:Mg^{2+} molar ratio of the synthesized sample was detected by using an ICP-OES 720 (Varian).

3. Results and discussion

The initial characterization of the produced nanocube specimen was performed by using SEM. Figure. 1a and 1b show SEM images of the $NaMn_{1-x}Mg_xF_3$@$NaMgF_3$ nanocube sample, indicating its uniformity and monodispersity. The particles have a regular cubic shape and have a narrow size distribution with an average width of *ca*. 288 nm (Figure. 1c). However, the particles are not monophasic single crystals as indicated by the powder X-ray diffraction (XRD) pattern in Figure 1d. The XRD pattern can be indexed to two phases. One, with diffraction peaks marked by the rhombus, is orthorhombic $NaMgF_3$ with a = 5.36, b = 7.68, and c = 5.50 Å (JCPDS card No. 13-0303). The other, marked by the asterisk, is close to orthorhombic $NaMnF_3$ (JCPDS card No. 18-1224, a =5.75, b = 8.00, and c = 5.55 Å) with all the observed diffraction peaks shifted slightly to higher 2θ angle, indicating a smaller unit cell. Both the phases can be regarded as $\sqrt{2} \times 2 \times \sqrt{2}$ superstructures derived from an ABO_3 perovskite subunit cell, in which all the O sites are replaced by F, the A sites are occupied by Na and the B sites by Mn or Mg.

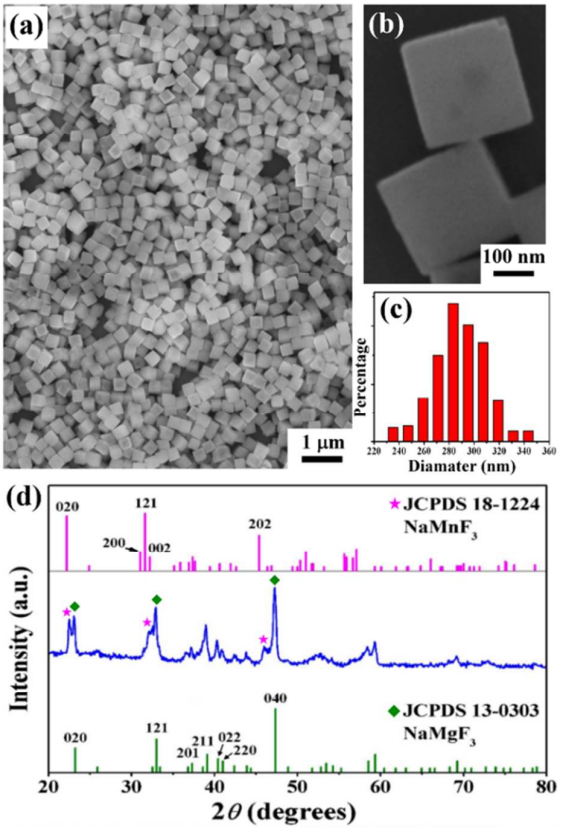

Figure 1. (a) Low- and (b) high-magnification SEM images of the nanocubes. (c) The size distribution of the particles. (d) The powder XRD pattern of the nanocubes in comparison with the standard patterns of $NaMgF_3$ and $NaMnF_3$.

Actually, both $NaMnF_3$ and $NaMgF_3$ have the same crystallographic structure. The smaller unit cell parameters of the latter are attributed to the smaller cation size of Mg^{2+} ions (ionic radius, r = 0.72 Å) than Mn^{2+} ions (r = 0.83 Å). The unit cell parameters of the first phase detected by XRD have been calculated using XRD pattern refinement (see Figure S3 for details in Supporting Information, SI) to be a = 5.6769, b = 7.8597, c = 5.5133 Å, falling in between the cell dimensions of $NaMnF_3$ and $NaMgF_3$. This phase is more likely due to a solid solution state of $NaMn_{1-x}Mg_xF_3$, in which Mn^{2+} in $NaMnF_3$ is partially substituted by Mg^{2+}. This conclusion has been supported by STEM experiments.

STEM was used to reveal the composition and microstructural features of the particles. The Z-contrast HAADF image of the nanocubes in Figure 2a shows their core-shell structures with a uniform thin shell thickness of approximate 40 ~ 50 nm, in which the core has a relatively higher brightness than the shell. It has been supported by the EDX elemental mapping of a typical nanocube as shown in Figure 2b. The difference in the elemental distribution of Mg and Mn over the whole nanocube unambiguously indicates a core-shell characteristic, in which Mn is located in the center region, while Mg is mainly at the periphery area. Na and F are observed in both the core and shell. This microstructure is illustrated in the inset model in Figure 2a.

Note that the lower contents of Na and F at the shell area may be resulted from the irradiation of the electron beam, leading to decomposition of the shell. Consequently, the shell has a relatively lower crystallinity or density than the core in the nanocubes under the examination. This phenomenon has also been observed from HRTEM images (Figure 2d). Based on the above results, it can be convinced that the nanocubes consist of a $NaMn_{1-x}Mg_xF_3$ core and a $NaMgF_3$ shell. The ICP result shows that the actual Mn^{2+}:Mg^{2+} molar ratio (25.25:100) is very close to the nominal Mn^{2+}:Mg^{2+} ratio (20:80).

As shown in Figure 2c, TEM image of the nanocubes also shows uniform particle size. The d-spacing of 0.381 nm as marked in the HRTEM image (Figure 2d) from a corner of a typical nanocube, which is mainly in the shell region, corresponds to the (020) planes of $NaMgF_3$. The corresponding selected area electron diffraction (SAED) pattern (the inset of Figure 2d), which can be indexed to orthorhombic $NaMgF_3$ along the $[10\bar{1}]$ zone axis, shows a single-crystalline nature of the shell. However, the outer surface layer of 3 to 4 nm in thickness has an obviously lower crystallinity. In addition, the diffraction spots corresponding to the 2-fold superlattice derived from the basic perovskite unit cell, e.g. the (010) diffraction spot, are also observed.

It is worth noting that the dropwise adding procedure of NaF solution played an important role in the formation of the core-shell structure. No core-shell structure was observed if 20 mL NaF solution was added at once (Figure S4 in SI). Unlike the

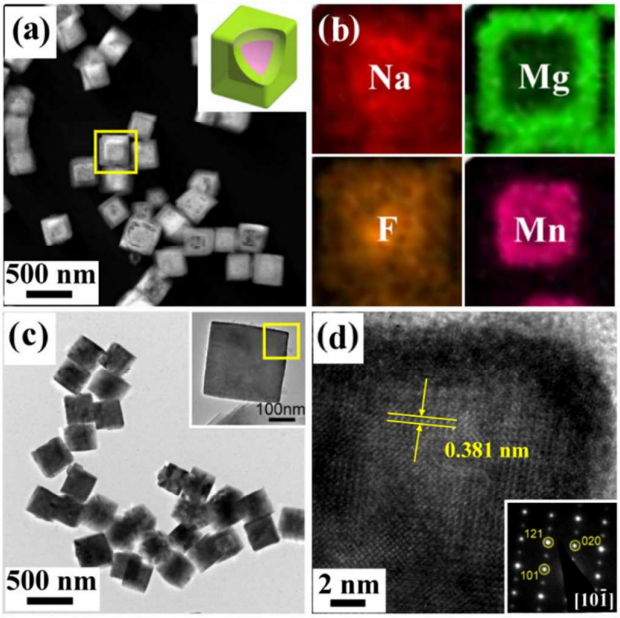

Figure 2. (a) HAADF-STEM image of the nanocubes. The inset is a schematic illustration of a core-shell structure synthesized with nominal molar ratio of Mn^{2+}:Mg^{2+} = 20:80. The $NaMgF_3$ shell is in green and the $NaMn_{1-x}Mg_xF_3$ core is in pink. (b) Component elemental maps from the nanocubic particle marked by the square in (a). (c) Low-magnification bright-field TEM image of the nanocubes. The inset is an enlarged TEM image of a typical nanocube. (d) HRTEM image and the corresponding SAED pattern (the inset) taken from the corner region marked by the square in (c).

core-shell nanocubes, only a single solid solution phase, which has the similar XRD pattern to the above perovskite phases, was detected in the sample. The refined unit cell parameters are a = 5.5387 Å, b = 7.7269 Å, c = 5.3952 Å (Figure S4a in SI). These values fall in the range of the corresponding unit cell parameters in between $NaMnF_3$ and $NaMgF_3$, with a good agreement with Vegard's law, when the nominal composition of $NaMn_{0.2}Mg_{0.8}F_3$ is taken account. [32, 33] SEM, TEM and SAED results indicate the sample is composed of single-crystalline but less regular nanocubes with a particle size of about 200 nm (Figure S4b-d in SI).

To investigate the morphological evolution of the products, a series of specimens with gradient addition of NaF have been collected and investigated. Based on the XRD results (Figure 3), we find that only tetragonal MgF_2 is detected at the early reaction stage after adding 10 mL NaF solution and it gradually reduces in content with further addition of NaF, indicating that MgF_2 is an intermediate phase. From TEM images, we find some irregular aggregates formed in the colloidal solution and many randomly orientated MgF_2 nanocrystallites (< 5 nm in diameter) are embedded in these particles (Figure 4).

As shown in Figure 5, an SAED pattern taken from a typical spherical aggregate shows that the particle contains polycrystalline MgF_2. The elemental mapping shows that both Mg and Mn co-exist in the particle. However, the surface areas are Mg rich, containing very low concentration of Mn. This indicates that the MgF_2 nanocrystallites are mainly located in

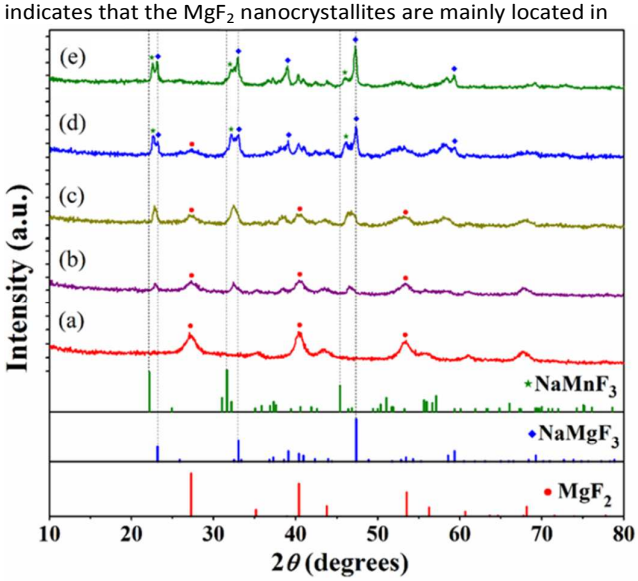

Figure 3. XRD patterns of the particles obtained with different amount of the NaF solution: (a) 10, (b) 12.5, (c) 15, (d) 17.5, (e) 20 mL. The standard XRD patterns (MgF2, JCPDS No.41-1443; NaMgF3, JCPDS No.13-0303; NaMnF3, JCPDS No. 18-1224) are also plotted for comparison.

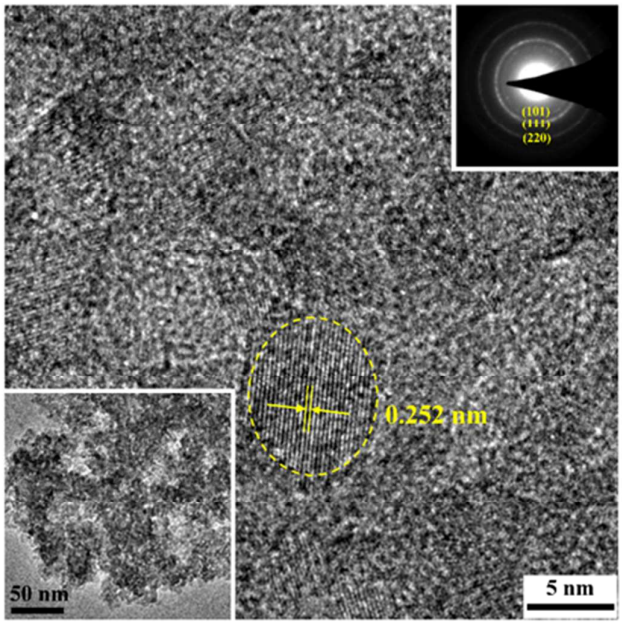

Figure 4. The HRTEM image of the MgF_2 nanocrystallites embedded in an amorphous matrix obtained by adding 10 mL NaF solution and the corresponding SAED patterns obtained from the whole section (up right inset). The left bottom inset is a low magnification TEM image. The measured interplanar spacing of 0.252 nm matches well with the (101) crystal planes of tetragonal MgF_2 (JCPDS card No. 41-1443).

near surface area. The experimental evidence allows us to propose that all the possible precursor molecules/ions, such as Na^+, F^-, Mn^{2+}, Mg^{2+} and acetate anions etc., firstly aggregated into amorphous spheres. Nucleation and development of nanocrystallites of MgF_2 took place inside these soft matter particles, more likely in the near-surface area. A

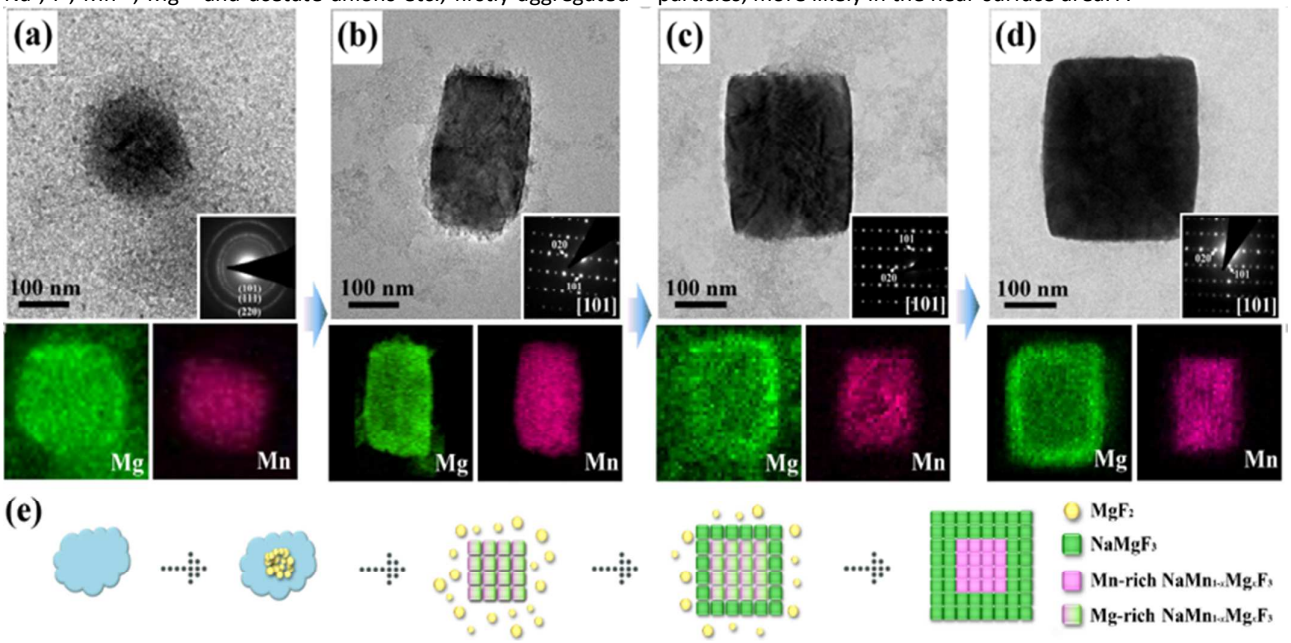

Figure 5. (a-d) TEM images and corresponding SAED patterns of particles obtained in a typical synthesis with different addi-tions of the NaF solution: (a) 10, (b) 12.5, (c) 15, and (d) 17.5 mL. The nominal Mn^{2+}:Mg^{2+} molar ratio is fixed at 20:80. The bottom insets are the Mg and Mn maps of the correspond-ing particles . (e) Schematic illustration of the formation mechanism for the core-shell nanocubes.

polymerization process plays an important role in such early stage aggregation, which is discussed in detail later.

When 12.5 mL NaF solution was added dropwise, the XRD pattern of the product (Figure 3b) reveals that, besides MgF_2, a new phase similar to the solid solution as shown in Figure S4a (in SI) appears. The SEM (Figure S5b in SI) and TEM images (Figures 5b and S6a in SI) reveal that the sample contains some quasi-rectangular particles. According to the single-crystal like SAED pattern taken from such an individual nanoparticle and its corresponding elemental mapping result (Figure 5b), the quasi-rectangular nanoparticle has a perovskite-type $NaMn_{1-x}Mg_xF_3$ solid solution structure. Since the particle size is similar to the MgF_2–containing spheres and the intensity of XRD peaks of MgF_2 decreases with the appearance of the solid solution phase, we believe that the $NaMn_{1-x}Mg_xF_3$ quasi-rectangular particles were developed from the MgF_2–containing particles due to further reactions of MgF_2 with Mn^{2+}, Na^+, and F^- inside the particles. The size difference between the distributed areas of Mg and Mn in the quasi-rectangular particles (Figure 5b) is less significant than that in the spherical particles (Figure 5a).

We also find that the crystallinity of the surface is higher than that in the inner part in the quasi-rectangular particles. The inner part is much more sensitive to electron beams and would be damaged more easily under the beam irradiation, while the surface layer is relatively stable, leading to a very thin crystalline box (Figure S6b-g in SI). The mesostructure is similar to an intermediate phase of zeolite A during a reversed crystal growth process.[34]

When more NaF was added, the intensity of XRD peaks of the perovskite solid solution phase increased (Figure 3c), and a new perovskite phase of $NaMgF_3$ was detected (Figure 3d). EDX elemental mapping reveals that Mn condenses in the central area of these particles (Figure 5c, d). Based on the above results, it can be concluded that a shell of $NaMgF_3$ has gradually developed on the surface of $NaMn_{1-x}Mg_xF_3$ particles, eventually forming $NaMn_{1-x}Mg_xF_3$@$NaMgF_3$ core-shell cubes. Moreover, a gradual increase in the intensity of XRD peaks of $NaMgF_3$ suggests that the crystallinity and thickness of $NaMgF_3$ shell is increasing with the increase of the addition of NaF solution (Figure 3). Furthermore, when zooming in the XRD patterns, we find that, with the addition of NaF, the diffraction peaks of solid solution phase gradually shift to lower diffraction angles, approaching to the peak positions of pure $NaMnF_3$ phase. It indicates that the content of Mg in $NaMn_{1-x}Mg_xF_3$ core decreases. In other words, Mg migrates from the $NaMn_{1-x}Mg_xF_3$ solid solution core to the surface, undergoing an in-situ phase transformation, which should be induced by the formation of the $NaMgF_3$ shell.

After adding 20 mL NaF solution, particles have a more regular cubic shape and smoother surface by consuming more precursor molecules/ions (Figure 1). The recrystallized surface of such an outer-shell is believed to have a higher crystallinity in comparison with the inner-core.

Consequently, the formation dynamic process of the core-shell nanocube architecture can be depicted as follows (schematically illustrated in Figure 5e).

Step 1, Aggregation of precursor molecules/ions. The aggregation forms amorphous spherical particles which may contain all types of existing ions and molecules, such as acetate anions (OAc^-), Mn^{2+}, Mg^{2+}, Na^+, F^-, and water. Considering the low dissociation constants of metal acetates, 1.2×10^{-10} for Mg acetate and 5.45×10^{-11} for Mn acetate, the principal forms of Mn and Mg in the solution are metal acetate tetrahydrate. Normally long chain molecules tend to gather into larger particles due to a strong interaction between the polymer molecules. However, there are no such large molecules in the synthetic solution. On the other hand, the six coordinated ligands, two OAc^- anions and four H_2O molecules, in the metal acetate molecules would be replaced by F^- anions step by step towards the formation of metal fluoride crystals. If this process is slow, a large number of dimers, $[OAc]_2 3H_2O$-M-F-M-$3H_2O[OAc]_2$ and polymers, $\{[OAc]_2 2H_2O$-M-F-$\}_n$ (where M = Mn or Mg) should be present in the solution. Charge balance of these polymerized long chain molecules is achieved by Na^+ cations. This type of polymers can aggregate easily due to its strong inter-molecular interaction and can be regarded as a growth base of MgF_2.

Step 2, Multiple nucleation of MgF_2 inside the aggregates and formation of MgF_2 nanocrystallites embedded in an amorphous matrix. The preferential formation of MgF_2 in contrast to MnF_2 is because of the much stronger Mg-F bonding than the Mn-F bonding. It can be confirmed by the much higher melting point of MgF_2 (1261 °C) than the MnF_2 (856 °C). On the other hand, 10 mL NaF solution (0.7 mol/L) supplied 7.0 mmol F^-, which is just enough to form MgF_2 corresponding to the total amount of 3.2 mmol Mg in the solution.

Step 3, Formation of $NaMn_{1-x}Mg_xF_3$ solid solution core. This phase was observed for the first time when 12.5 mL NaF was added. The molar ratio of Mn : Mg : F in the synthetic system is 0.8 : 3.2 : 8.75. Even all 4 mmol Mn and Mg formed MnF_2 and MgF_2, there are still 0.75 mmol excess F left. The crystal phase of MF_2 would undergo a phase transformation to perovskite $NaMF_3$ in this step and excess F can be consumed. Consequently, the reduction of MgF_2 in this sample can be understood. The particles with the $NaMn_{1-x}Mg_xF_3$ solid solution phase are polycrystalline as seen on the TEM images (Figure S4b in SI), but all the nanocrystallites in the particles seem to be self-orientated, giving single crystal like SAED patterns (Figures 5b, S4c in SI).

Step 4, Surface re-crystallization to form a thin shell of $NaMgF_3$. In the perovskite phase, the tolerant factor for $NaMnF_3$ is 0.76 and that for $NaMgF_3$ is 0.81. It seems to be true that $NaMgF_3$ has less distortion and its formation is easier than $NaMnF_3$. As we observed in many systems, the surface of disordered aggregates is more active in re-crystallization when a reversed crystal growth takes place. [35, 36] At this stage, the core is still polycrystalline with all the crystallites are self-orientated, therefore, the SAED patterns look like single crystals. Under electron beam irradiation, the self-ordering can be broken so that the corresponding SAED patterns look like polycrystalline, but the single crystal shell of $NaMgF_3$ is maintained (Figure S6 in SI).

Step 5, Further phase transformation of the solid solution core to form core-shell nanocubes. Due to different degrees of lattice distortion in $NaMnF_3$ and $NaMgF_3$, partially substituting Mn by Mg in the former or Mg by Mn in the latter would introduce extra lattice tension. When the crystallites in the solid solution core are small, this type of tension can be relaxed near surface. However, a purer phase with less distortion would grow preferentially when the crystals become larger. Therefore, an extension of re-crystallization of $NaMgF_3$ shell and migration of Mg from inner $NaMn_{1-x}Mg_xF_3$ solid solution phase to the outer $NaMgF_3$ would dominate the subsequent phase transformation process of the core to finally form $NaMn_{1-x}Mg_xF_3$@$NaMgF_3$ core-shell nanocubes. In many solid solution metal oxides, ordering or partial ordering of the guest ions occurs to form some superstructures. These superstructures may not create visible diffraction peaks in the XRD patterns. But they can be easily detected by SAED. [37,38] Absence of any extra diffraction spots in the SAED patterns of $NaMn_{1-x}Mg_xF_3$ indicates that the substitution of Mn^{2+} by Mg^{2+} in this solid solution is completely random.

To further understand the formation mechanism of the unique $NaMgF_3$:Mn^{2+}@$NaMgF_3$ core-shell nanostructure in this case, we also performed theoretical calculations on the 2×2×2 supercell of $NaMgF_3$ with two Mg^{2+} ions replaced by two Mn^{2+} ions, and the total number atoms of the supercell are 160. According to the Figure S1 and S2, when two Mg^{2+} ions are replaced by two Mn^{2+} ions, there are fifteen different substitution geometry models (denoted as M1-M15). The DFT calculation results were given in Table S2. It can be clearly observed that the different substitution geometries would posses different total energy. Particularly, the total energies of M1 and M2 are significantly lower than others. While, the total energies of the others are very close. These facts indicate the substitution geometries of M1 and M2 are more preferable in Mn^{2+} doped $NaMgF_3$, that is, the Mn^{2+} ions in $NaMgF_3$ tend to show an unevenly distribution. More interestingly, in models of M1 and M2, the shortest Mn^{2+}-Mn^{2+} distances are both about ~3.8 Å, which are much lower than all of the others, and $\{Mn^{2+}$-F-$Mn^{2+}\}$ unit can be formed, suggesting that Mn^{2+} ions preferable to aggregation in $NaMgF_3$:Mn^{2+}. Therefore, besides the external experimental conditions, the aggregation tendency of Mn^{2+} ions in $NaMgF_3$ should also be considered as one of reasons for forming the unique $NaMgF_3$:Mn^{2+}@$NaMgF_3$ core-shell nanostructure. In this structure, as $\{Mn^{2+}$-F-$Mn^{2+}\}$ unit would appear, in addition, the Mn^{2+}-Mn^{2+} distance is of ~3.8 Å, super-exchange coupled Mn^{2+}-Mn^{2+} emission center can be also be expected. [19, 39]

As a proof-of-concept experiment for producing NIR upconvension (UC) luminescence of Mn^{2+} through using the novel core-shell nanocubes, Yb^{3+} ions were doped into this structure. Note that there is almost no change in phase and core-shell morphology for these Yb-doped samples before and after calcination (Figures S7-9 in SI). Moreover, the Yb^{3+} ions tend to evenly both distribute into core $NaMn_{1-x}Mg_xF_3$ and shell $NaMgF_3$, therefore the novel core-shell structure $NaMn_{1-x}Mg_xF_3$:Yb^{3+}@$NaMgF_3$:Yb^{3+} has been obtained (see Figure S9). Under 976 nm laser excitation, greatly enhanced visible and

infrared UC emissions were observed for the samples after a low temperature heat treatment (Figure 6, Figure S10a in SI). The visible UC emission band centered at 600 nm corresponds to the $^2F_{7/2}$, $^4T_{1g}(G) \rightarrow {}^2F_{7/2}$, $^6A_{1g}(S)$ transition of the Yb^{3+}-Mn^{2+} pairs, and the near infrared emission band at ~780 nm may be due to transition from Yb^{3+}-Mn^{2+}-Mn^{2+} clusters. [40] Based on the power dependent UC emissions, it can be known that both visible and NIR UC emissions belong to a two-photons UC process (see Figure S11).[23] In addition, the body colour is of the sample is white, while the UC luminescence colour is orange, as shown in Figure S12. The extremely weak emission for the samples before heat treatment may be due to the presence of the luminescence quencher in the form of an O-H group (Figure S10b). [41] Thus, the post-heat treatment was needed to promote UC luminescent intensity.

To further validate the effectiveness of the core-shell structure for enhancing the near infrared UC through Mn-Mn aggregation effect, we prepared two other samples with an equal content of Mn^{2+} besides the Yb-doped core-shell structure (sample CS). They are solid solution $NaMn_{0.2}Mg_{0.8}F_3$: 0.5mol% Yb^{3+} nanocrystals (sample SS) and the physically mixed biphase $(0.2)NaMnF_3/(0.8)NaMgF_3$:0.5mol%$Yb^{3+}$ (sample PM) (Figure S13). The distribution of Mn^{2+} in these samples is well controlled with a random doping, an aggregation in the core area, and a pure $NaMnF_3$. The UC emission spectra of the three samples upon excitation by a 976 nm laser diode are shown in Figure 6.

The UC emission spectra with two peaks at approximately 600 and 780 nm are observed in these samples except for the physically mixed biphasic samples, meaning that a pure phase cannot produce efficient UC emission. More interestingly, the

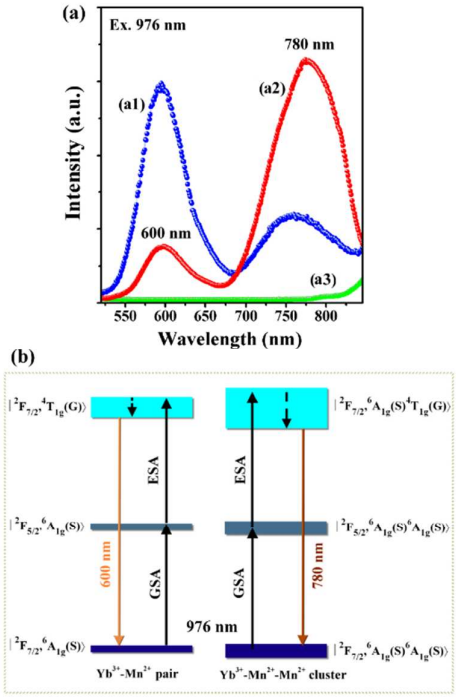

Figure 6. (a) UC emission spectra of (a1) sample SS, (a2) sample CS (red) and (a3) sample PM (green) upon a 976 nm laser diode excitation. (b) Possible schematic energy level the core-shell structured sample. The core shell sample (a2) and solid solution sample (a1) were both synthesized with a nominal Yb^{3+}:Mn^{2+}:Mg^{2+} molar ratio of 0.5:20:80.

spectra of Mn^{2+} show different emission profiles although they synthesized with a same nominal Yb^{3+}:Mn^{2+}:Mg^{2+} molar ratio of 0.5:20:80, and the UC emission at 780 nm (originated from $|\,{}^2F_{7/2}, {}^6A_{1g}(S)\ {}^4T_{1g}(G)\rangle \rightarrow |\,{}^2F_{7/2}, {}^6A_{1g}(S)\ {}^6A_{1g}(S)\rangle$ transition) in CS sample as is much stronger than that of SS sample. [40] The VIS and NIR UC emissions can be ascribed to ground state absorption (GSA) and excited state absorption (ESA) two photon upconversion luminescence processes (Fig. 6b). Moreover, based on the UC emission spectra shown in Fig.6, the relative intensity of the two emission bands (～600 and ～780 nm) and the total emission intensity for the CS and SS samples have been given in Figure S14. It can be observed that the visible emission (~600 nm) intensity was decreased by 73% in CS sample as compared to that of SS sample. Whereas the emission intensity of NIR emission band was enhanced by 129%. The selectively enhanced the NIR UC emission is due to the change of Mn^{2+} distribution in CS sample as compared to that of SS sample. Meanwhile, the total emission intensity of the CS sample was improved by 9.4% is mainly ascribed to the reduction of surface defects. These findings give a direct evidence for Mn^{2+}-Mn^{2+} aggregation induced NIR UC emission at the single particle level. It is noticed that this mechanism for enhancing UC emission is different in nature compared to the lanthanide-doped nanoparticles in which a high concentration of dopant usually results in declined emission.[41] Notably, because the near infrared emission just within the "optical transparency window" of biological tissues (700−1100 nm), the novel core-shell structures hold great potential for applications in deep-penetration and high-resolution bioimaging. [43, 44]

4. Conclusions

In summary, we report a simple one-pot, surfactant-free co-precipitation method for synthesizing core-shell structured $NaMn_{1-x}Mg_xF_3$@$NaMgF_3$ and $NaMn_{1-x}Mg_xF_3$:Yb^{3+}@$NaMgF_3$:Yb^{3+} nanocubes at room temperature. By taking advantage of electron microscopic analysis and EDX elemental mapping of the samples obtained at different stages during the reaction, the formation mechanism, consisting of aggregation of precursor molecules/ions, multiple nucleation, surface re-crystallization and further phase transformation, has been elucidated. Moreover, the DFT calculations further showed that Mn^{2+} ions tend to aggregate in $NaMgF_3$:Mn^{2+}, and which may be one of important intrinsic factors for formation the unique $NaMn_{1-x}Mg_xF_3$@$NaMgF_3$ structure in this case. Although part of the crystal growth route, including aggregation, multiple nucleation, surface re-crystallization, etc. were previously observed in other materials, e.g. $BaTiO_3$,[45] the microstructure with a solid solution core and a single crystalline shell, and the role of the core as a reservoir to

supply building materials for the shell, is very interesting. The formation mechanism of the core-shell nanocubes provides a new model system for studying the self-construction of core-shell nanostructures. Remarkably enhanced near infrared upconvension of Mn^{2+} were realized under excitation by a 976 nm laser diode for the 0.5 mol% Yb^{3+}-doped core-shell nanocubes after a facile post-heat treatment, compared to the corresponding solid solution nanoparticles. We believe this study can provide an insight into the one-pot, low-cost aqueous phase synthesis of core-shell nanocomposites and promote their applications in near infrared bioimaging and catalysis.

Acknowledgements

This work is financially supported by the National Natural Science Foundation of China (Grant No. 51125005, 51472088, 51602104).

References

1 R. Ghosh Chaudhuri and S. Paria, *Chem. Rev.*, 2011, **112**, 2373.
2 B. Zhou, B. Shi, D. Jin and X. Liu, *Nat. Nanotechnol.*, 2015, **10**, 924.
3 J. T. Xu, A. Gulzar, Y. H. Liu, H. T. Bi, S. L. Gai, B. Liu, D. Yang, F. He and P. P. Yang, *Small*, 2017, **13**, 1701841.
4 G. X. Yang, D. Yang, P. P. Yang, R. C. Lv, C. X. Li, C. G. Zhong, F. He, S. L. Gai and J. Lin, *Chem. Mater.*, 2015, **27** , 7957.
5 S. L. Gai, C. X. Li, P. P. Yang and J. Lin, *Chem. Rev.*, 2014, **114**, 2343.
6 G. Y. Chen, H. L. Qiu, P. N. Prasad and X. Y. Chen, *Chem. Rev.*, 2014, **114**, 5161.
7 J. Zhou, Z. Liu and F. Y. Li, *Chem. Soc. Rev.*, 2012, **41**, 1323.
8 F. Wang, R. R. Deng, J. Wang, Q. X. Wang, Y. Han, H. M. Zhu, X. Y. Chen and X. G. Liu, *Nat. Mater.*, 2011, **10**, 968.
9 M. Haase and H. Schäfer, *Angew. Chem., Int. Ed.*, 2011, **50**, 5808.
10 G. S. Yi and G. M. Chow, *Chem. Mater.*, 2007, **19**, 341.
11 S. W. Wu, G. Han, D. J. Milliron, S. Aloni, V. Altoe, D. V. Talapin, B. E. Cohen and P. J. Schuck, *Proc. Natl. Acad. Sci. U. S. A.*, 2009, **106**, 10917.
12 F. Wang, J. Wang and X. Liu, *Angew. Chem., Int. Ed.*, 2010, **49**, 7456.
13 B. Zhou, W. F. Yang, S. Y. Han, Q. Sun and X. G. Liu, *Adv. Mater.*, 2015, **27**, 6208.
14 G. Chen, H. Agren, T. Y. Ohulchanskyy and P. N. Prasad, *Chem. Soc. Rev.*, 2015, **44**, 1680.
15 X. Chen, D. Peng, Q. Ju and F. Wang, *Chem. Soc. Rev.*, 2015, **44**, 1318.
16 X. Li, D. Shen, J. Yang, C. Yao, R. Che, F. Zhang and D. Zhao, *Chem. Mater.*, 2013, **25**, 106.
17 C.-H. Kuo, T.-E. Hua and M. H. Huang, *J. Am. Chem. Soc.*, 2009, **131**, 17871.
18 J. H. Yu, S.-H. Kwon, Z. Petrášek, O. K. Park, S. W. Jun, K. Shin, M. Choi, Y. I. Park, K. Park, H. B. Na, N. Lee, D. W. Lee, J. H. Kim, P. Schwille and T. Hyeo, *Nat. Mater.*, 2013, **12**, 359.
19 C. Barthou, J. Benoit, P. Benalloul and A. Morell, *J. Electrochem. Soc.*, 1994, **141**, 524.
20 C. Bertail, S. Maron, V. Buissette, T. Le Mercier, T. Gacoin and J.-P. Boilot, *Chem. Mater.*, 2011, **23**, 2961.
21 R. Beaulac, P. I. Archer, S. T. Ochsenbein and D. R. Gamelin, *Adv. Funct. Mater.*, 2008, **18**, 3873.
22 G. G. Li and J. Lin, *Chem. Soc. Rev.*, 2014, **43**, 7099.
23 E. Song, S. Ye, T. Liu, P. Du, R. Si, X. Jing, S. Ding, M. Peng, Q. Zhang and L. Wondraczek, *Adv. Sci.*, 2015, **2**, 1500089.
24 E. H. Song, J. L. Wang, S. Ye, X. B. Yang M. Y. Peng, Q. Y. Zhang and L. Wondraczek, *Adv. Opt. Mater.*, 2017, **5**, 201700070.
25 J. Q. Hu, E, H, Song, S, Ye, B, Zhou and Q. Y. Zhang, *J. Mater. Chem. C*, 2017, **5**, 3343.
26 Y. Zhang, J. D. Lin, V. Vijayaragavan, K. K. Bhakoo and T. T. Y. Tan, *Chem. Commun.*, 2012, **48**, 10322.
27 G. Kresse and J. Furthmüller, Phys. Rev. B: Condens. Matter Mater. Phys., 1996, **54**, 11169.
28 G. Kresse and D. Joubert, *Phys. Rev. B: Condens. Matter Mater. Phys.*, 1999, **59**, 1758.
29 Z. Li, W. Xu, Y. Yu, H. Du, K. Zhen, W. Wang, L. Luo, H. Qiu and X. Yang, *J. Mater. Chem. C*, 2016, **4**, 362.
30 J. P. Perdew, K. Burke and M. Ernzerhof, *Phys. Rev. Lett.*, 1996, **77**, 3865.
31 E. H. Song, Y. Y. Zhou, X.-B. Yang, Z. F. Liao, W. R. Zhao, T. T. Deng, L. Y. Wang, Y. Y. Ma, S. Ye, Q. Y. Zhang, ACS Photonics, 2017, **4**, 2556.
32 L. Vegard, *Zeit. Physik.*, 1921, **5**, 17.
33 F. J. Yu and W. Z. Zhou, *Prog. Nat. Sci. Mater. Int.*, 2013, **23**, 331.
34 J. F. Yao, D. Li, X. Y. Zhang, C. H. Kong, W. B. Yue, W. Z. Zhou and H. T. Wang, *Angew. Chem., Int. Ed.*, 2008, **47**, 8397.
35 H. Greer, P. S. Wheatley, S. E. Ashbrook, R. E. Morris and W. Z. Zhou, *J. Am. Chem. Soc.*, 2009, **131**, 17986.
36 K. Self, H. J. Zhou, H. F. Greer, Z. R. Tian and W. Z. Zhou, *Chem. Commun.*, 2013, **49**, 5411.
37 W. Zhou, *J. Solid State Chem.*, 1988, **76**, 290.
38 W. Zhou, D. A. Jefferson, M. Alario-Franco and J. M. Thomas, *J. Phys. Chem.*, 1987, **91**, 512.
39 A. P. Vink, M. A. de Bruin, S. Roke, P. S. Peijzel and A. Meijerink, *J. Electrochem. Soc.*, 2001, **148**, E313.
40 E. H. Song, S. Ding, M. Wu, S. Ye, F. Xiao, S. F. Zhou and Q. Y. Zhang, *Adv. Opt. Mater.*, 2014, **2**, 670.
41 M. N. Luwang, R. S. Ningthoujam, S. K. Srivastava and R. K. Vatsa, *J. Am. Chem. Soc.*, 2011, **133**, 2998.
42 X. M. Li, R. Wang, F. Zhang and D. Y. Zhao, *Nano Lett.*, 2014, **14**, 3634.
43 J. Zhou, Y. Sun, X. X. Du, L. Q. Xiong, H. Hu and F. Y. Li, *Biomaterials*, 2010, **31**, 3287.
44 G. Chen, T. Y. Ohulchanskyy, R. Kumar, H. Agren and P. N. Prasad, *ACS Nano*, 2010, **4**, 3163.
45 H. Zhan, X. Yang, C. Wang, J. Chen, Y. Wen, C. Liang, H. F. Greer, M. Wu and W. Zhou, *Cryst. Growth Des.*, 2012, **12**, 1247.

An Efficient synthetic Strategy for Uniform Perovskite Core-Shell Nanocubes $NaMgF_3:Mn^{2+}$, Yb^{3+}@$NaMgF_3:Yb^{3+}$ with Enhanced Near Infrared Upconversion Luminescence

S. Ding,[a#] X. F. Yang,[b#] E. H. Song,[a] C. L. Liang,[c] B. Zhou,[a] M, M, Wu,[c] W, Z, Zhou,[d] and Q. Y. Zhang*[a]

[a.] *State Key Laboratory of Luminescent Materials and Devices, and Institute of Optical Communication Materials, South China University of Technology, Guangzhou 510640, P. R. China*

[b.] *Analytical and Testing Center, South China University of Technology, Guangzhou 510640, P. R. China*

[c.] *School of Chemistry and Chemical Engineering, and Instrumental Analysis and Research Centre, Sun Yat-Sen (Zhongshan) University, Guangzhou 510275, P. R. China*

[d.] *EaStCHEM, School of Chemistry, University of St Andrews, St Andrews, Fife KY16 9ST, United Kingdom*

[1)] Author to whom correspondence should be addressed; Email: qyzhang@scut.edu.cn

Table S1. Optimized lattice constants for a 2×2×2 $NaMgF_3$ supercell.

Lattice constants	Value
a (Å)	10.7459
b (Å)	11.0440
c (Å)	15.3944
α(degree)	90.0000
β(degree)	90.0000
γ(degree)	90.0000
V(Å^3)	1826.9722

Table S2. The shortest Mn-Mn distance and total energy (E_0) of fifteen proposed substitution geometry models for a 2×2×2 supercell of $NaMgF_3$:Mn^{2+} with two Mg^{2+} ions replaced by two Mn^{2+} ions.

Model	Mn-Mn distance (Å)	E_0 (eV)
M1	3.8523	-797.7180
M2	3.8486	-797.7080
M3	5.4453	-797.6124
M4	5.37295	-797.6159
M5	6.6091	-797.6145
M6	5.4453	-797.6154
M7	5.5220	-797.6149
M8	6.7308	-797.6136
M9	7.7046	-797.6095
M10	8.6123	-797.6162
M11	7.6971	-797.6136
M12	8.6074	-797.6152
M13	9.3870	-797.6159
M14	9.4731	-797.6149
M15	10.8907	-797.6125

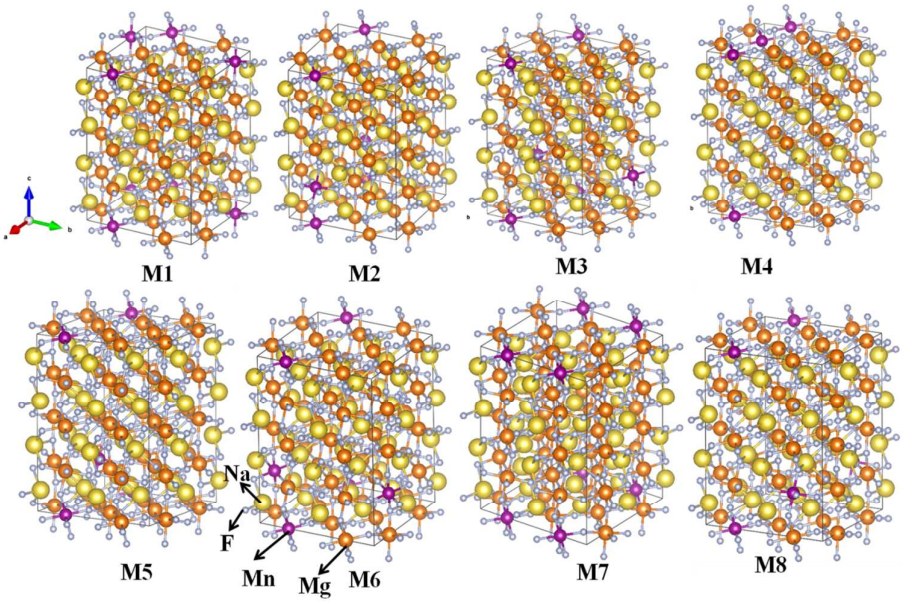

Figure S1. Possible substitution geometry models (denoted as M1-M8) for a 2×2×2 supercell of $NaMgF_3$:Mn^{2+} with two Mg^{2+} replaced by two Mn^{2+}.

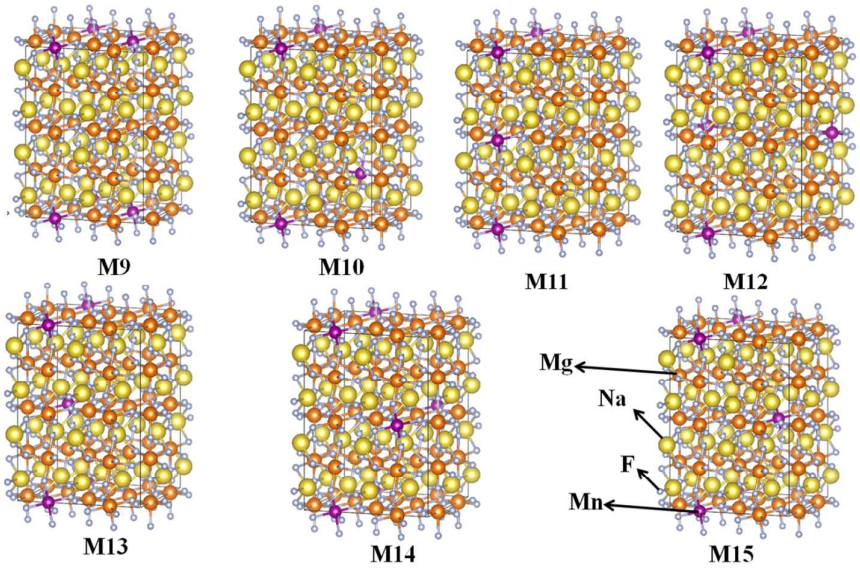

Figure S2. Possible substitution geometry models (denoted as M9-M15) for a 2×2×2 supercell of $NaMgF_3$:Mn^{2+} with two Mg^{2+} replaced by two Mn^{2+}.

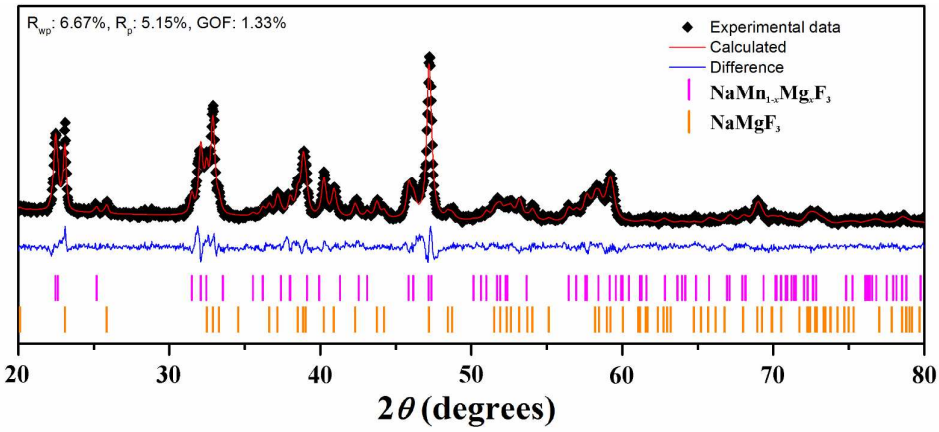

Figure S3. Rietveld refinement of powder XRD profile of $NaMn_{1-x}Mg_xF_3$@$NaMgF_3$ core-shell nanocubes shown in Figure 1.

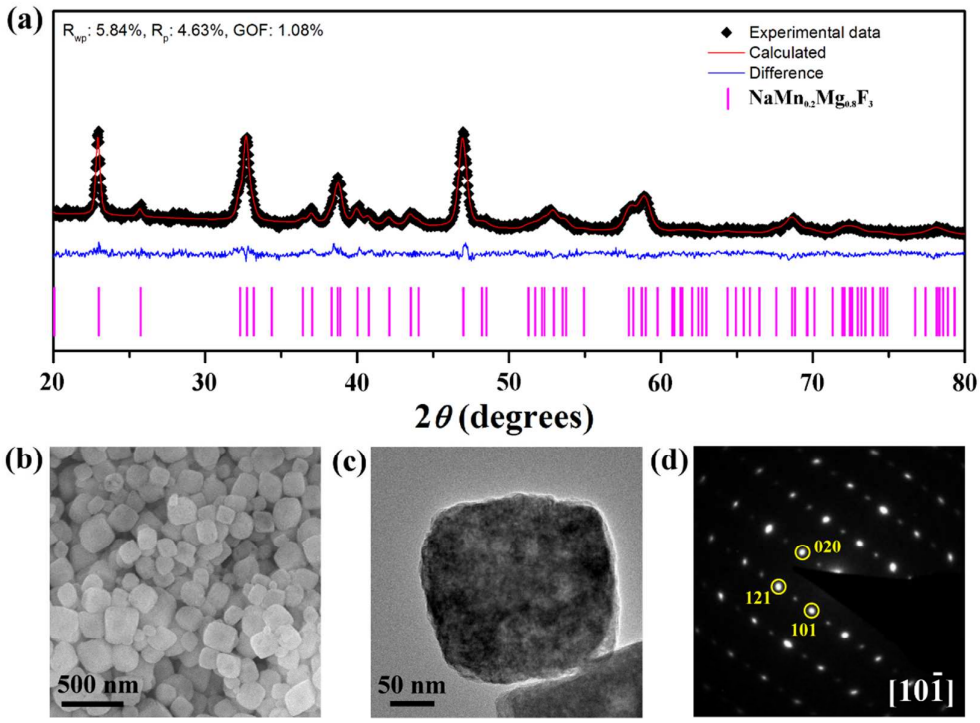

Figure S4. (a) Rietveld refinement of powder XRD profile of solid-solution $NaMn_{0.2}Mg_{0.8}F_3$ nanoparticles prepared by adding all the NaF solution as once. (b) Low-magnification SEM image and (c) high-magnification TEM image of the nanoparticles, and (d) the SAED pattern taken from the corresponding whole particle of (c).

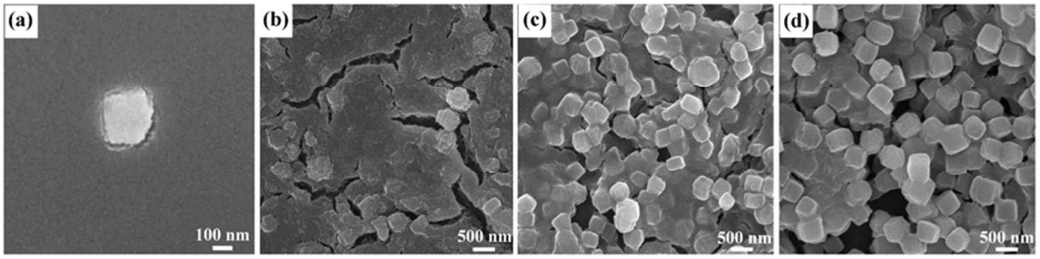

Figure S5. SEM images of the particles obtained with different additions of NaF solution amounts: (a) 10 mL; (b) 12.5 mL; (c) 15 mL; (d) 17.5 mL.

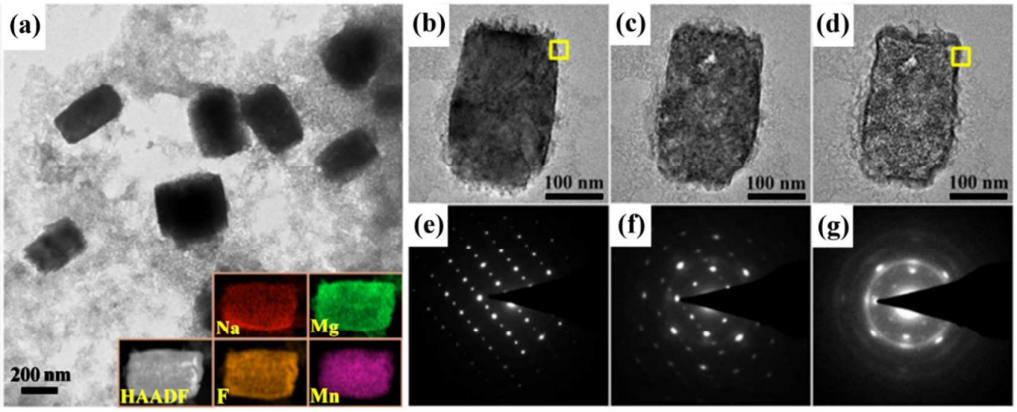

Figure S6. (a) TEM image of the particles obtained in a typical synthesis of nanocubes with 12.5 mL NaF solution. The insets of (a) show an HAADF image and the component element maps of a particle. (b-d) TEM images of the same particle after electron beam irradiation for a few minutes: (c) 2 minutes; (d) 10 minutes. The corresponding SAED patterns are shown below (e-g).

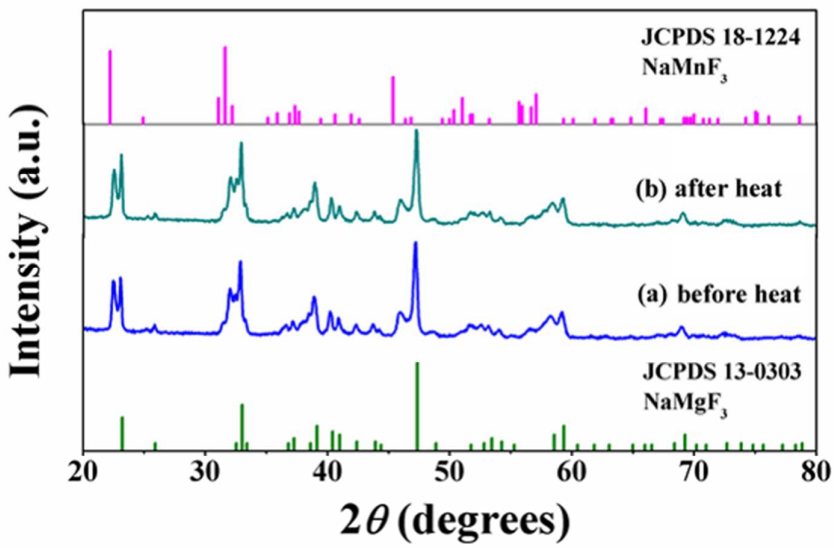

Figure S7. XRD pattern of $NaMn_{1-x}Mg_xF_3:Yb^{3+}$@$NaMgF_3:Yb^{3+}$ core-shell nanocubes synthesized with a nominal Yb^{3+}:Mn^{2+}:Mg^{2+} molar ratio of 0.5:20:80 before (a) and after (b) the thermal treatment for 2 h in comparison with the standard patterns of $NaMnF_3$ and $NaMgF_3$.

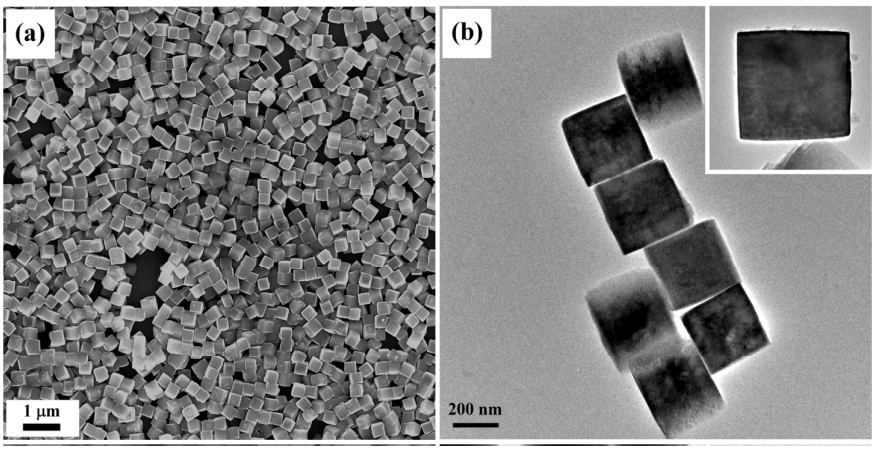

Figure S8. Typical (a) SEM and (b) TEM images of $NaMn_{1-x}Mg_xF_3:Yb^{3+}$@$NaMgF_3:Yb^{3+}$ nanostructures synthesized with a nominal Yb^{3+}:Mn^{2+}:Mg^{2+} molar ratio of 0.5:20:80 before heat treatment.

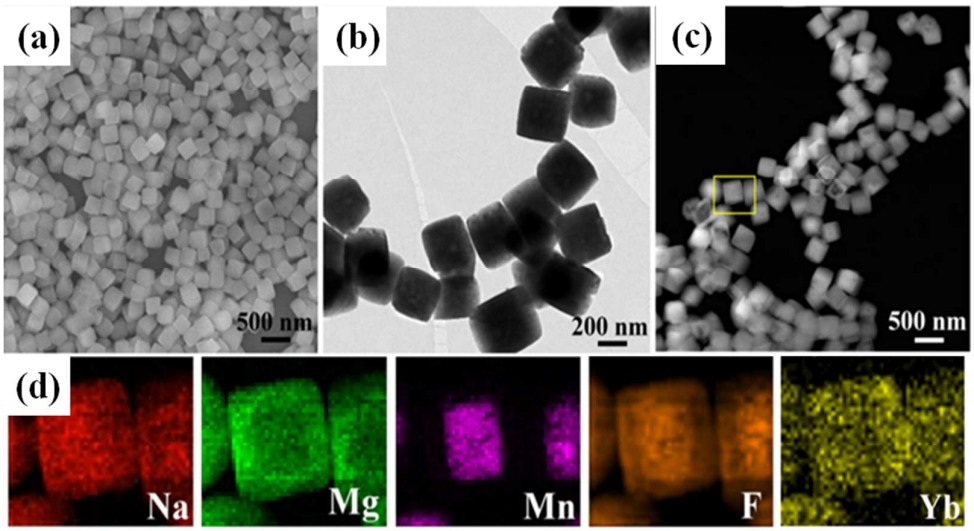

Figure S9. (a) SEM image and (b) TEM image of $NaMn_{1-x}Mg_xF_3:Yb^{3+}$@$NaMgF_3:Yb^{3+}$ core-shell nanocubes s. (c) HAADF image of a large area of the nanocubes and (d) the component element maps of the marked area in (c).

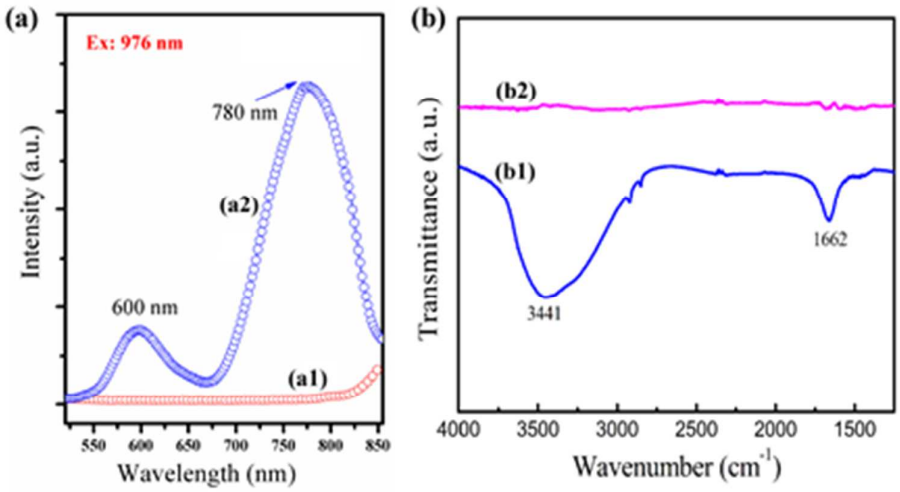

Figure S10. (a) Upconvension emission spectra of the $NaMn_{1-x}Mg_xF_3:Yb^{3+}$@$NaMgF_3:Yb^{3+}$ core-shell nanocubes before (a1) and after (a2) heat treatment upon 976 nm laser diode excitation, respectively. (b) FT-IR spectra of the core-shell nanocubes before (b1) and after (b2) heat treatment, respectively. The broad absorption band (the blue lines) located at 3441 and 1662 cm^{-1} can be associated with the O–H stretching vibration of water and almost disappear after the thermal treatment (the pink lines).

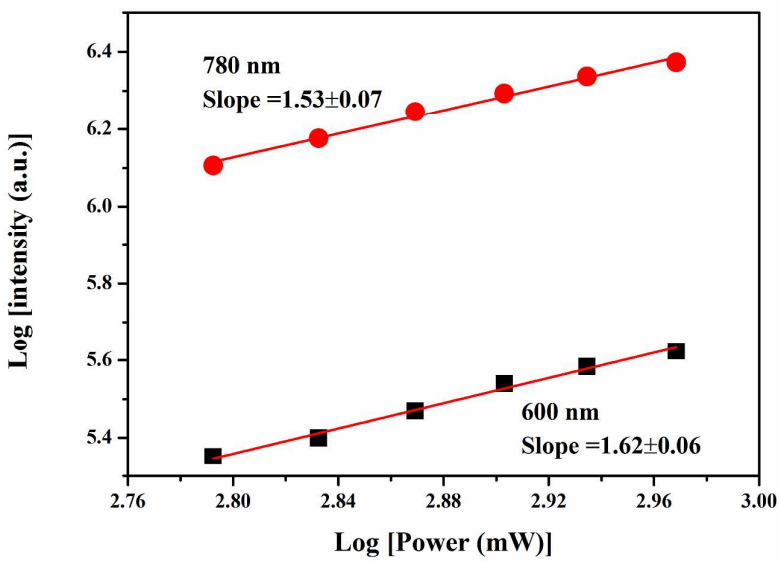

Figure S11. Log-log plots of upconversion emission intensities of visbile and NIR emissions as a function of pump power in $NaMg_{1-x}Mn_xF_3:Yb^{3+}@NaMgF_3:Yb^{3+}$ synthesized with a nominal Yb^{3+}:Mn^{2+}:Mg^{2+} ratio is 0.5:20:80. We use the pumper dependent UC emissions, the slopes for the visible and NIR emissions are determined to be about 1.62±0.06 and 1.53±0.07 (Fig.4.), respectively, which confirms that both visible and NIR UC emission bands in this system belong to two photons Upconversion processes.

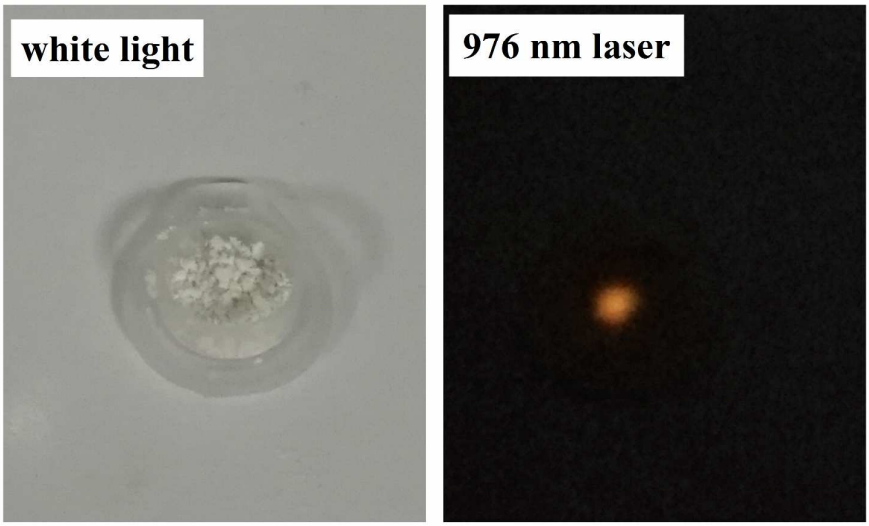

Figure S12. Pictures of novel $NaMn_{1-x}Mg_xF_3:Yb3+@NaMgF_3:Yb^{3+}$ core-shell structure synthesized with a nominal Yb^{3+}:Mn^{2+}:Mg^{2+} ratio of 0.5:20:80 under white light radiation and 976 nm laser excitation, respectively.

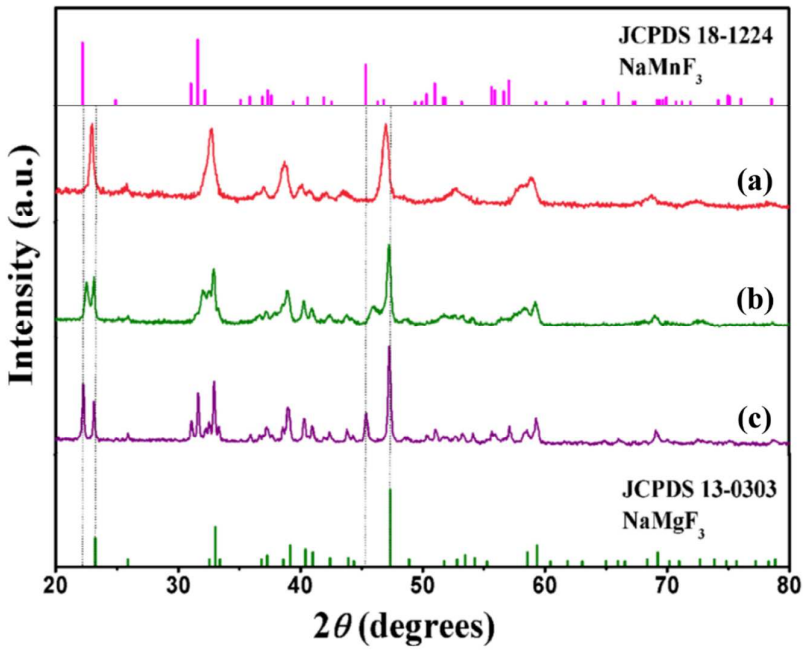

Figure S13. XRD patterns of the particles obtained with the reactive species ratio (Mn^{2+} to Mg^{2+} molar ratio) of 1 : 4 through different synthetic processes. (a) Solid solution $NaMn_{0.2}Mg_{0.8}F_3$: 0.5mol%Yb^{3+} (sample SS), (b) core-shell $NaMn_{1-x}Mg_xF_3$:Yb^{3+}@$NaMgF_3$:Yb^{3+} (sample CS), (c) physically-mixed 0.2$NaMnF_3$/0.8$NaMgF_3$: 0.5mol%Yb^{3+} (sample PM).

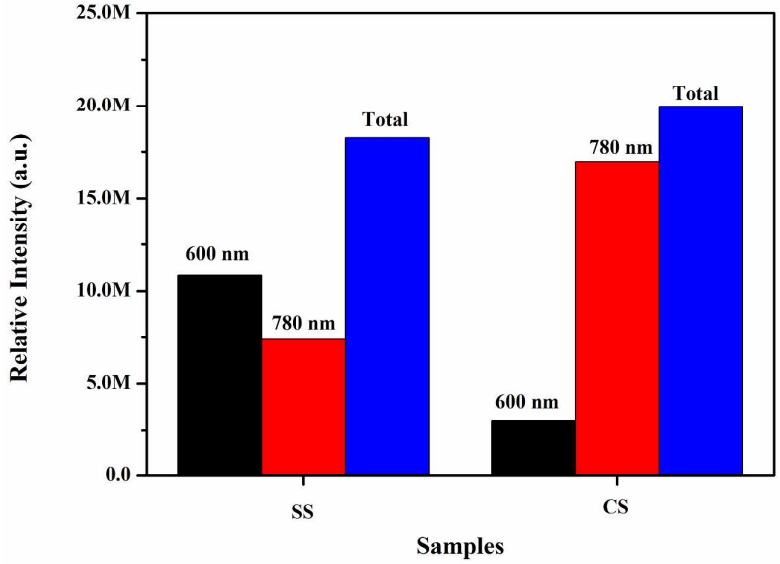

Figure S14. The relative upconversion luminescence intensity of the 600 nm, 780 nm and the total of the two emission bands in CS and SS samples under the same measure condition.